

# Preparation of GQDs/TiO<sub>2</sub> nanotube heterojunction photoanode and its photoelectrochemical performance for water splitting

Zhizhong Xiao<sup>#</sup>, Shengye Cheng<sup>#</sup>, Wenbo Liao, Dayong Fan<sup>\*</sup>, Huidan Lu<sup>\*</sup>, and Yongping Liu

Guangxi Key Laboratory of Electrochemical and Magneto-chemical Functional Materials, College of Chemistry and Bioengineering, Guilin University of Technology, Guilin 541004, P. R. China.

<sup>#</sup>These authors contributed equally to this work

<sup>\*</sup>E-mail: [dyfan@glut.edu.cn](mailto:dyfan@glut.edu.cn) (Fan D); [lhuidangl@163.com](mailto:lhuidangl@163.com) (Lu H)

Received: 24 April 2022 / Accepted: 23 May 2022 / Published: 4 July 2022

Photoelectrochemical (PEC) water splitting is a promising technology for converting solar energy into hydrogen energy. This paper fabricated a GQDs/TiO<sub>2</sub> nanotube heterojunctions photoanode by graphene quantum dots (GQDs) assisted anodization method. SEM, TEM, XRD, XPS, FIRT, Raman spectroscopy characterized its morphology and structure. Results demonstrated that graphene quantum dots were incorporated into the TiO<sub>2</sub> film layer to form GQDs/TiO<sub>2</sub> nanotube array heterojunctions. The introduction of GQDs enhanced the absorption of visible light and significantly improved the charge carrier density from  $9.073 \times 10^{19} \text{ cm}^{-3}$  to  $1.265 \times 10^{21} \text{ cm}^{-3}$ , compared with the TiO<sub>2</sub> nanotube array. As a result, the PEC behavior of GQDs/TiO<sub>2</sub> nanotube arrays is greatly improved. Under a bias voltage of 0.8 V, the photocurrent density of the GQDs/TiO<sub>2</sub> heterojunction photoanode is 5 times higher than that of the pure TiO<sub>2</sub> nanotube array. This work provides an important reference for developing high-efficiency PEC water splitting photoanode.

**Keywords:** Photoelectrochemical, TiO<sub>2</sub>, nanotube, graphene quantum dots, heterojunction

## 1. INTRODUCTION

Hydrogen energy would be expected to replace traditional fossil fuels due to the non-pollution and renewable advantages [1, 2]. Splitting water for hydrogen production using sunlight is an ideal strategy to solve energy and environmental issues.[3, 4] TiO<sub>2</sub> has attracted extensive attention for photocatalytic hydrogen evolution since it was first reported in the photocatalytic field[5]. TiO<sub>2</sub> nanotube arrays have advantages of large specific surface area, excellent charge transport properties, non-toxicity, high catalytic activity, chemical stability, and low cost. They are promising photoanode materials with significant application prospects[6-8]. Although the stability of TiO<sub>2</sub> is high enough, due to the large bandgap (rutile: 3.0 eV, anatase: 3.2 eV)[9, 10], it can only absorb ultraviolet light 4%-5% of the sunlight.

To improve the utilization of the sun, enhancing visible light absorption to facilitate the separation of photogenerated carriers is the key to strengthening photocatalytic efficiency[11].

Doping is a crucial method for tuning the properties of catalyst materials [12-14]. Changing the type and content of doping atoms can adjust the bandgap and conductivity of semiconductor materials, thereby altering their optoelectronic properties. Therefore, selecting appropriate doping elements and the amount is critical for regulating photoelectric properties. So far, the doping elements used to improve the photoelectric activity of  $\text{TiO}_2$  include C, N, Sn, Sr, Nb, etc.[15-18]. Bian et al.[19] prepared  $\text{TiO}_2$ /graphene composites by one-step hydrothermal method. The transport mode of the photo-induced carrier in composites can effectively accelerate the separation of electrons and holes. Xu's group[20] obtained Sn-doped  $\text{TiO}_2$  nanowires by hydrothermal method, and the photocurrent of  $\text{TiO}_2$ /Sn material was nearly doubled that of pure  $\text{TiO}_2$  nanowires. Kavitha Pandi et al.[21] have proved that carbon doping and metal nitrate hydroxide support enhanced the light absorption and the separation/transportation of photo-generated charge carriers of  $\text{TiO}_2$ . However, it is limited that enhancing visible light absorption and improved electrode conductivity by the doping method cannot significantly strengthen PEC performance. Constructing a heterojunction combines one semiconductor with another conductor (such as noble metal and carbon material) to form a composite photo-electrode material, increasing visible light absorption and promoting photo-generated light charge separation and transport[22, 23]. Cheng's group[24] revealed that the hole injection efficiency of the  $\text{BiVO}_4/\text{TiO}_2/\text{FTO}$  photoanode is inferior to that of the bare  $\text{BiVO}_4/\text{FTO}$  anode for oxygen evolution. Swetha S.M.Bhat et al.[25] studied the photoelectrochemical (PEC) water splitting properties of two-dimensional (2D)  $\text{MoS}_2$  nanosheets (NSs) modified 1D  $\text{TiO}_2$  nanorods/0D CdS nanocrystals (NCs) heterojunction and found that  $\text{MoS}_2$  NSs transfer holes from CdS and facilitate further charge separation in  $\text{TiO}_2$ /CdS. Jiang's team[26] reported a one-pot hydrothermal method was adopted to assemble Ag nanoparticles and nitrogen-doped graphene (NGR) onto  $\text{TiO}_2$  to form NGR/Ag- $\text{TiO}_2$  composites. Ascribe to the decoration of Ag nanoparticles and NGR, the exciton lifetime was lengthened, and charge transfer was improved. As a result, the transient photocurrent intensity of the as-prepared nanocomposites is 18.2 times higher than that of pristine  $\text{TiO}_2$ . Li [27] et al. fabricated  $\text{TiO}_2$ /nanographite composite photoelectrode materials using the sol-gel method. Nanographite with 2-3 nm thickness was uniformly anchored on the surface of anatase  $\text{TiO}_2$  of 10 nm thickness to constitute  $\text{TiO}_2$ /nanographite heterojunctions. The charge transfer resistance of the electrode dropped sharply, and the transient photocurrent was 10.5 times that of  $\text{TiO}_2$ . Wang's group[28] has demonstrated that  $\text{TiO}_2$ /Au thin films have good absorption capacity and high photocurrent response under visible light irradiation, suggesting doping Au nanoparticles can stimulate the PEC activity of  $\text{TiO}_2$  materials.

In this paper, GQDs were first dispersed in the electrolyte, and then  $\text{TiO}_2$  nanotubes were grown on the titanium sheet's surface by anodic oxidation. During anodic oxidation, graphene quantum dots and titanium dioxide symbiotic together to constitute GQDs/ $\text{TiO}_2$  nanotube heterojunctions, which worked as a photoanode for water splitting. It is studied that the effect of GQDs on PEC performance of  $\text{TiO}_2$  nanotubes array.

## 2. EXPERIMENT

### 2.1 Preparation of graphene quantum dots (GQDs)

All reagents were analytical grade and purchased from Shanghai Reagents Company (Shanghai, China). GQDs were prepared by hydrothermal method[29]. In a typical procedure, Firstly, 2.00 g of pyrene (purity > 98%) and 160 ml of concentrated nitric acid (AR grade) were mixed. Then the mixture solution was refluxed under stirring for 12 h in an electric heating constant temperature water bath at 80 °C so that the nitration reaction occurred. After the reaction was completed, it was cooled to room temperature, and 1 L of deionized water was added to dilute the H<sup>+</sup> in the solution. The reacted solution was filtered with a microporous membrane of  $\phi$ M 0.22  $\mu$ m. After drying in a vacuum oven at 60 °C for 10 h, about 3 g of yellow intermediate product 1,3,6-trinitropyrene was obtained. 0.30 g of 1,3,6-trinitropyrene was dissolved in 60 mL 0.20 mol/L of NaOH solution, sonicated for 2 h, and then hydrothermally reacted at 200 °C for 10 h. After the reaction was completed, it was cooled down and filtered with a microporous membrane of  $\phi$ M 0.22  $\mu$ m. The filtrate was dialyzed in distilled water using a dialysis bag (MD44 mm) for two days, and the water was changed 5 to 6 times during this period. Finally, about 8.48 mg/mL of graphene quantum dots (GQD-OH) with hydroxyl groups were obtained.

### 2.2 Preparation of TiO<sub>2</sub> Nanotubes and GQDs/TiO<sub>2</sub> Nanotube Heterojunctions

Preparation of TiO<sub>2</sub> NTs[30]: A titanium foil (1cm × 4 cm) was sonically cleaned for 15 min in acetone, ethanol, and deionized water successively before the anodization. The washed titanium sheets were dried at 60°C for use. The TiO<sub>2</sub> NTs were synthesized by electrochemical anodization in a glycol electrolyte solution containing 0.2 wt % NH<sub>4</sub>F and 0.6 wt % H<sub>2</sub>O at 60 V for 90 minutes. Then, the as-prepared samples were dried in ambient air after being rinsed with ethanol and deionized water. Finally, the as-prepared samples were annealed in the atmosphere at 500 °C for 2 h, and the TiO<sub>2</sub> NTs were obtained.

Preparation of GQDs/TiO<sub>2</sub> NTs heterojunctions: 5 mL, 10 mL, 15 mL, and 20 mL of graphene quantum dots were added to the anodized electrolyte to anodize the titanium sheets. Except for adding different amounts of graphene quantum dots, other experimental procedures are the same as the preparation mentioned above of TiO<sub>2</sub> NTs. The as-obtained samples were denoted as GQDs/TiO<sub>2</sub>-5, GQDs/TiO<sub>2</sub>-10, GQDs/TiO<sub>2</sub>-15 and GQDs/TiO<sub>2</sub>-20, respectively.

### 2.3 Characterization

The crystal structures of the as-synthesized samples were characterized by PANalytical X'Pert PRO X-ray diffraction (XRD) with Cu K $\alpha$  radiation ( $\lambda = 1.5418 \text{ \AA}$ ) in the range of 10 to 90°. The microstructures of the as-prepared samples were characterized by scanning electron microscopy (SEM, JSM-638OLV) and transmission electron microscopy (TEM, JEOL, JEM-2100F). The UV-vis absorption spectra of the samples were measured by a UV/VIS/NIR Spectrometer (PerKinElmer, Lambda 750) at 200 to 800 nm. BaSO<sub>4</sub> was used as the standard reflectance material. The ESCALAB

250Xi system took the X-ray Photoelectron Spectroscopy (XPS). The binding energy for the C 1s peak at 284.6 eV was used as the reference for calibration. Raman spectra were taken by Thermo Fisher scientific.

#### 2.4 Photoelectrochemical property measurements

The photoelectrochemical properties have been investigated using a three-electrode system on an electrochemical workstation (CHI 660E, CH Instruments). Using silicone rubber, all the as-prepared samples were fabricated to a 1 cm × 1 cm area. Then, the fabricated samples were used as a photoanode, with a Pt wire as a counter electrode and a saturated calomel electrode (SCE) as a reference electrode in a 0.5 M Na<sub>2</sub>SO<sub>4</sub> solution (pH=6.8) to set up a three-electrode system. The illumination source (Beijing Perfectlight Technology Co., CHF-XM 500W Xe lamp) was calibrated to one sun (100mW cm<sup>-2</sup>) using a spectroradiometer (Beijing Au-light Co., CEL-NP2000). The photocurrent-potential measurement was recorded from -0.2 to 0.8 V *vs.* SCE at a scan rate of 0.01 V s<sup>-1</sup>, and the light was chopped manually at regular intervals. The amperometric i-t curves were measured at the bias potential of 0.5 V *vs.* SCE. Mott-Schottky plots were measured at a frequency of 1000 Hz in the dark. The measured potential *vs.* SCE was converted to the reversible hydrogen electrode (RHE) scale by using the Nernst equation:[31]

$$E(\text{RHE}) = E(\text{SCE}) + 0.059 \times \text{pH} + 0.2412\text{V}$$

### 3. RESULTS AND DISCUSSION

Fig. 1 shows the XRD patterns of TiO<sub>2</sub> NTs and GQDs/TiO<sub>2</sub> NTs composites samples with different GQDs loadings (5 mL, 10 mL, 15 mL, 20 mL). It can be seen from Fig.1 that the as-obtained TiO<sub>2</sub> NTs are composed of anatase phase TiO<sub>2</sub> with good crystallinity (JPDS card No. 73-1764). The diffraction peak positions of GQDs/TiO<sub>2</sub> NTs composites are the same as pure TiO<sub>2</sub> NTs, implying that the crystal phase of TiO<sub>2</sub> does not change after GQDs are added. But with the increase of GQDs content, the intensity of the diffraction peaks gradually weakens, suggesting a decrease in the crystallinity of TiO<sub>2</sub>. At the same time, the diffraction peak of GQDs at 26.43° is not observable, which may be due to less GQDs content that leads to a weak diffraction peak covered by the peak of TiO<sub>2</sub> at 25.4°.

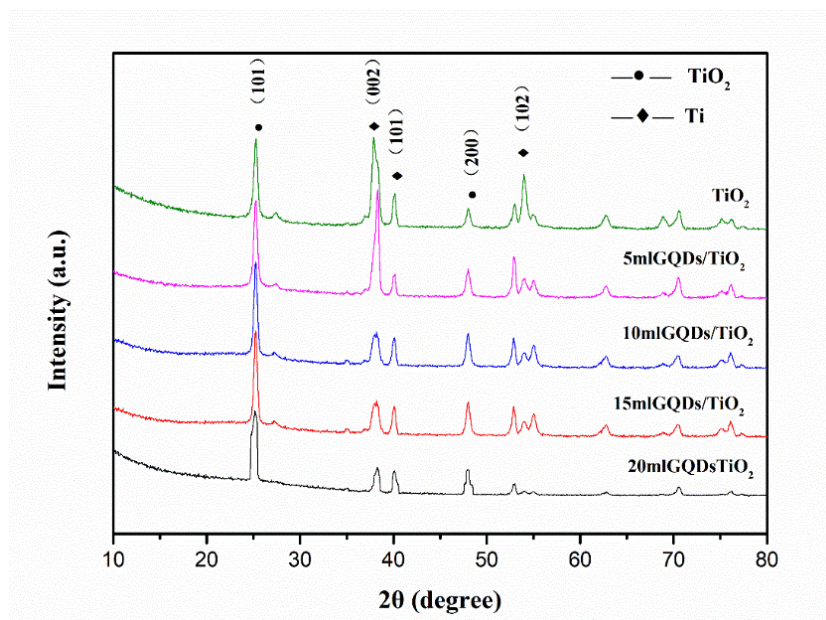


**Figure 1.** XRD patterns of  $\text{TiO}_2$  NTs and GQDs/ $\text{TiO}_2$  NTs composites

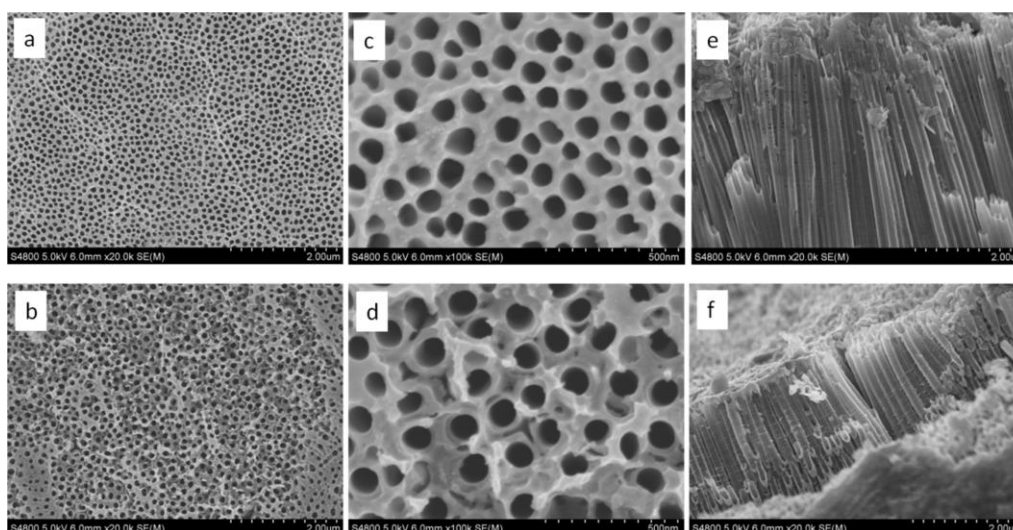


**Figure 2.** The SEM images of  $\text{TiO}_2$  NTs (a, c, e) and GQDs/ $\text{TiO}_2$  NTs composites (b, d, f). The top SEM images (a-d) and the cross-section SEM images (e-f)

The SEM images of  $\text{TiO}_2$  and GQDs/ $\text{TiO}_2$  samples are present in Fig. 2. It can be seen from Fig. 2 (a, c, e) that the as-prepared  $\text{TiO}_2$  has an ordered tubular structure with a diameter of about 50~100 nm, and the wall thickness is 20-30 nm. Fig. 2 (b, d, f) shows the microscopic morphology, diameter, and wall thickness of GQDs/ $\text{TiO}_2$  samples are almost identical to pure  $\text{TiO}_2$  NTs, which revealed that the addition of graphene quantum dots during anodization didn't affect the growth of  $\text{TiO}_2$  nanotubes. To further verify the distribution of GQDs in  $\text{TiO}_2$  nanotubes, TEM characterization of GQDs/ $\text{TiO}_2$  NTs samples at different magnification was measured. Fig. 3 (a, b) exhibits a tubular structure of  $\text{TiO}_2$ , with a 20~30 nm diameter and the lattice spacing of 0.462 nm corresponds to (102) crystal plane of  $\text{TiO}_2$ . Moreover, Fig. 3 (c, d) is a TEM image of GQDs/ $\text{TiO}_2$  NTs composites, there are some small black dots

with a diameter of about 3~8 nm uniformly dispersing in the lattice fringes of the TiO<sub>2</sub>, denoting that GQDs exist inside and on the surface of TiO<sub>2</sub> nanotubes.

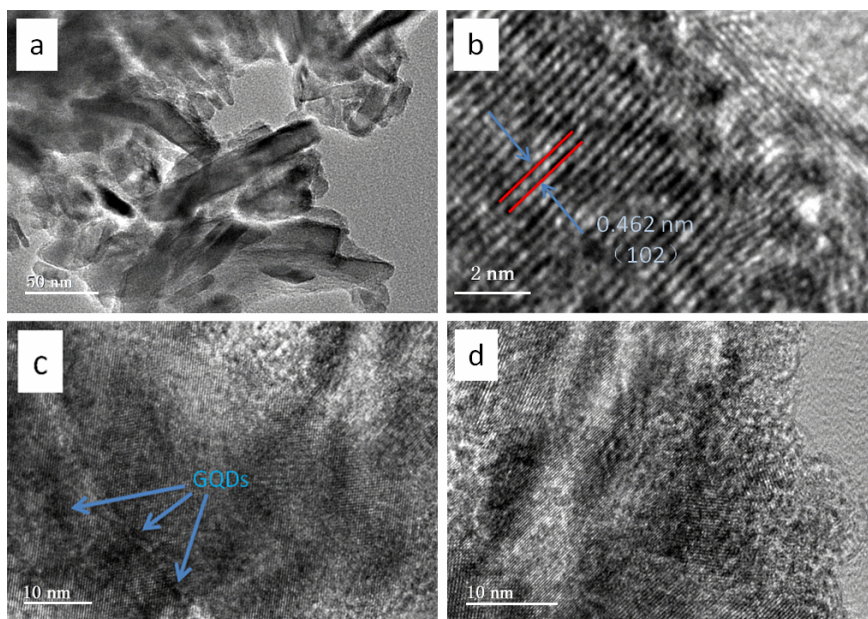


**Figure 3.** The TEM images of TiO<sub>2</sub> NTs (a, b) and GQDs/TiO<sub>2</sub> NTs composites (c, d)

X-ray photoelectron spectroscopy (XPS) is an effective means for analyzing the chemical states of elements. Figure 4 is the XPS spectrum of the GQDs/TiO<sub>2</sub> composites sample. The overall XPS spectrum of the sample (Fig. 4a) shows that the GQDs/TiO<sub>2</sub> composite sample is composed of three elements Ti, O, and C. Fig. 4b shows the spectrum of Ti 2p, which shows Ti 2p has two characteristic peaks at 458.5 eV and 464.3 eV, attributed to Ti 2p<sub>3/2</sub> and Ti 2p<sub>1/2</sub>, respectively. The difference in binding energy between two peaks is 5.8 eV, signifying characteristics of tetravalent titanium[32]. There are two peaks of O 1s in Fig. 4c, among which the strong peak at 529.59 eV is the Ti-O bond energy, and the peak at 531.33 eV corresponds to C-O in GQDs-OH. The XPS spectrum of carbon elements (Fig. 4d) displays that the peaks at 288.2 eV and 284.6 eV are assigned to C-O and C=C of GQD-OH, respectively. Therefore, the above analysis of chemical binding energy concluded that the graphene quantum dots had been successfully embedded in the TiO<sub>2</sub> nanotube array.

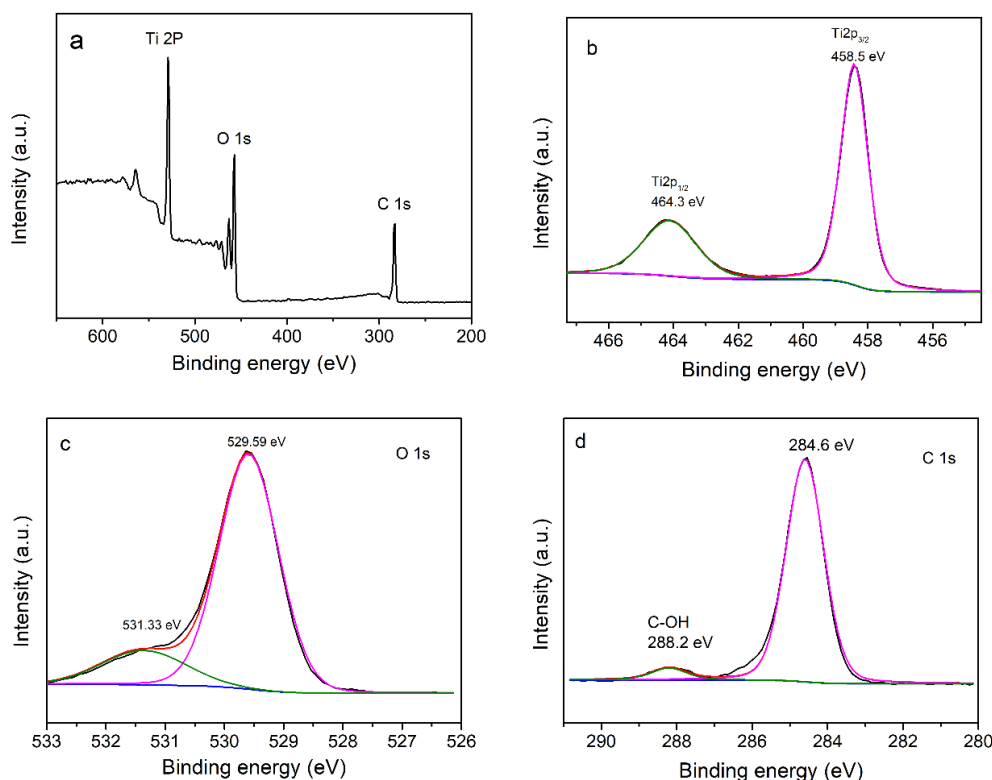


**Figure 4.** (a) XPS survey spectrum of GQDs/TiO<sub>2</sub>, (b) Ti 2p, (c) O 1s, (d) C 1s

To further confirm the combination of GQDs and TiO<sub>2</sub> nanotubes, the Raman spectra of GQDs/TiO<sub>2</sub> were tested, as shown in Fig. 5e. It has been reported[33, 34] that Raman signals of graphene quantum dots are similar to graphene, with distinct D and G peaks around  $\sim 1325\text{ cm}^{-1}$  and  $\sim 1585\text{ cm}^{-1}$ . Compared with the pristine TiO<sub>2</sub> nanotubes array, the Raman spectrum of GQDs/TiO<sub>2</sub> nanotube heterojunctions shows two new peaks: D and G peaks, assigned to disordered carbon structure (sp<sup>3</sup>) and ordered graphitic carbon (sp<sup>2</sup> clusters), respectively[35, 36], belonging to GQDs. Results testified during the anodization process; the GQDs have entered the interior of the structure of the TiO<sub>2</sub> nanotube.

The UV-Vis diffuse reflectance absorption spectra of TiO<sub>2</sub> and GQDs/TiO<sub>2</sub> composites (Fig. 5a) exhibits that the absorption band edge of TiO<sub>2</sub> is around 380 nm, while that of GQDs/TiO<sub>2</sub> is red-shifted to 390 nm. A bandgap of 3.16 eV, which matches well with previous reports (3.2 eV for anatase), is extracted from the plot (Fig. 5b)[37]. However, the bandgap of GQDs/TiO<sub>2</sub>-20 is plotted to be 3.04 eV, which is narrower than pure TiO<sub>2</sub> nanotubes. Furthermore, from Fig. 5a, visible light absorption is significantly enhanced by increasing graphene quantum dots added. Results suggested that the addition of GQDs can broaden the absorption range of TiO<sub>2</sub> nanotubes and strengthen the absorption of visible light.

The PEC properties of TiO<sub>2</sub> and TiO<sub>2</sub> nanotube composites with different contents of GQDs were measured in a three-electrode system under simulated solar illumination on/off switching. Fig. 5c-d shows that photocurrent rises instantly for both TiO<sub>2</sub> nanotubes and GQDs/TiO<sub>2</sub> nanotube composites upon illumination. Once the light illumination quenches, it sharply drops to zero, signifying that the samples have a superior PEC responsiveness. In Fig. 5c, an apparent decay trend of photocurrent can be

observed under the applied voltage of 0.8 V for TiO<sub>2</sub> and GQDs/TiO<sub>2</sub>-5. While, with the increase of GQDs amount, photocurrent density for the GQDs/TiO<sub>2</sub> samples tends to be stable. For example, there is no detectable photo-response attenuation for GQDs/TiO<sub>2</sub>-20 following the next photo-switching cycle. Results revealed that the modification of graphene quantum dots could play an essential role in stabilizing the PEC water splitting performance of TiO<sub>2</sub>. Additionally, after 400 s, the photogenerated current density of TiO<sub>2</sub> reached a stable value of 14 μA/cm<sup>2</sup>, and that of GQDs/TiO<sub>2</sub>-20 was 72 μA/cm<sup>2</sup>, which is 5.14 times higher than that of the former and is the highest value among all of GQDs/TiO<sub>2</sub> composites under the same conditions. It is demonstrated that the construction of GQDs modified TiO<sub>2</sub> nanotube structure can significantly boost the photoelectrochemical activity. In addition, carefully observing Fig. 5d, we can also find that the photocurrent density of the composites gradually rises with the increase of GQDs loaded. It is speculated that heterojunction formation could reduce the recombination efficiency of photogenerated electron-holes. Additionally, the unique combination of GQDs and TiO<sub>2</sub> nanotubes would induce a strong binding force, enhancing the migrating speed of photogenerated charges. The PEC response and stability of TiO<sub>2</sub> nanotubes are strengthened due to the introduction of GQDs.

Both the flat-band potential ( $E_{FB}$ ) and the charge carrier density ( $N_D$ ) are the most critical parameters for studying the equilibrium state of the electrode/electrolyte interface, and the Mott-Schottky theory can derive these two parameters. To elucidate the electron transport mode of the semiconductor interface, we tested the Mott-Schottky curves of TiO<sub>2</sub> nanotubes and GQDs/TiO<sub>2</sub>.

Equation (1) [37] indicates that the capacitance  $C$  of the space charge layer has a linear relationship with the electrode potential  $E$ .

$$\frac{1}{C_{sc}^2} = \frac{2}{e_0 \varepsilon_0 \varepsilon_r N_D} [-Where] \quad (1)$$

Where,  $C_{sc}$  is the space charge capacitance in the semiconductor,  $e_0$  is the electronic charge,  $\varepsilon_0$  is the vacuum permittivity,  $\varepsilon_r$  is the relative permittivity,  $N_D$  is the charge carrier density,  $E$  is the applied potential,  $E_{FB}$  is the flat-band potential,  $k$  is the Boltzmann constant, and  $T$  is the absolute temperature. From Fig. 5f, the flat band potentials of TiO<sub>2</sub> and GQDs/TiO<sub>2</sub> electrodes can be calculated as -0.26 V and -0.55 V vs. SCE, respectively. Converting the reference electrode from SCE to standard hydrogen electrode (NHE) by adding 0.24 V (25°C), the flat band potential of GQDs/TiO<sub>2</sub> is -0.31 V vs. NHE, negative than that of TiO<sub>2</sub> (-0.02 V vs. NHE), implying a lower external bias to drive the PEC reaction.

The charge carrier density  $N_D$  is calculated by equation (2) [38]:

$$N_D = \frac{2}{e_0 \varepsilon_0 \varepsilon_r} \left[ \frac{d\frac{1}{C^2}}{dV} \right]^{-1} \quad (2)$$

Equation (2) declares that the smaller the slope of the linear part of the MS curve is, the higher the carrier density is at the electrode interface. According to the Mott-Schottky plots, the slopes of TiO<sub>2</sub> and GQDs/TiO<sub>2</sub> are estimated to be  $1.092 \times 10^{10}$  and  $1.523 \times 10^9$ , respectively. The relative permittivity  $\varepsilon$  of TiO<sub>2</sub> is equal to 170 reported in references[39]. By formula (2), the charge carrier density of TiO<sub>2</sub> can be derived to be  $9.073 \times 10^{19}$  cm<sup>-3</sup>, and that of GQDs/TiO<sub>2</sub> is  $1.265 \times 10^{21}$  cm<sup>-3</sup>, which is two orders of magnitude higher than the former. The carrier density of GQDs/TiO<sub>2</sub> composite nanotube arrays enhanced significantly, manifesting the increased electronic conductivity and the efficient

photogenerated charge transfer and separation owing to the introduction of GQDs. Compared with similar photoanode materials used for water splitting, GQDs/TiO<sub>2</sub> composites have superior PEC properties (as shown in table 1). For example, the enhancement rate of the current density of GQDs/TiO<sub>2</sub> photoanode materials is 514%, higher than other materials listed in table 1 except for rGQDs/Fe<sub>2</sub>O<sub>3</sub>. And its charge carrier density is the largest among all the photoanode materials in table 1.

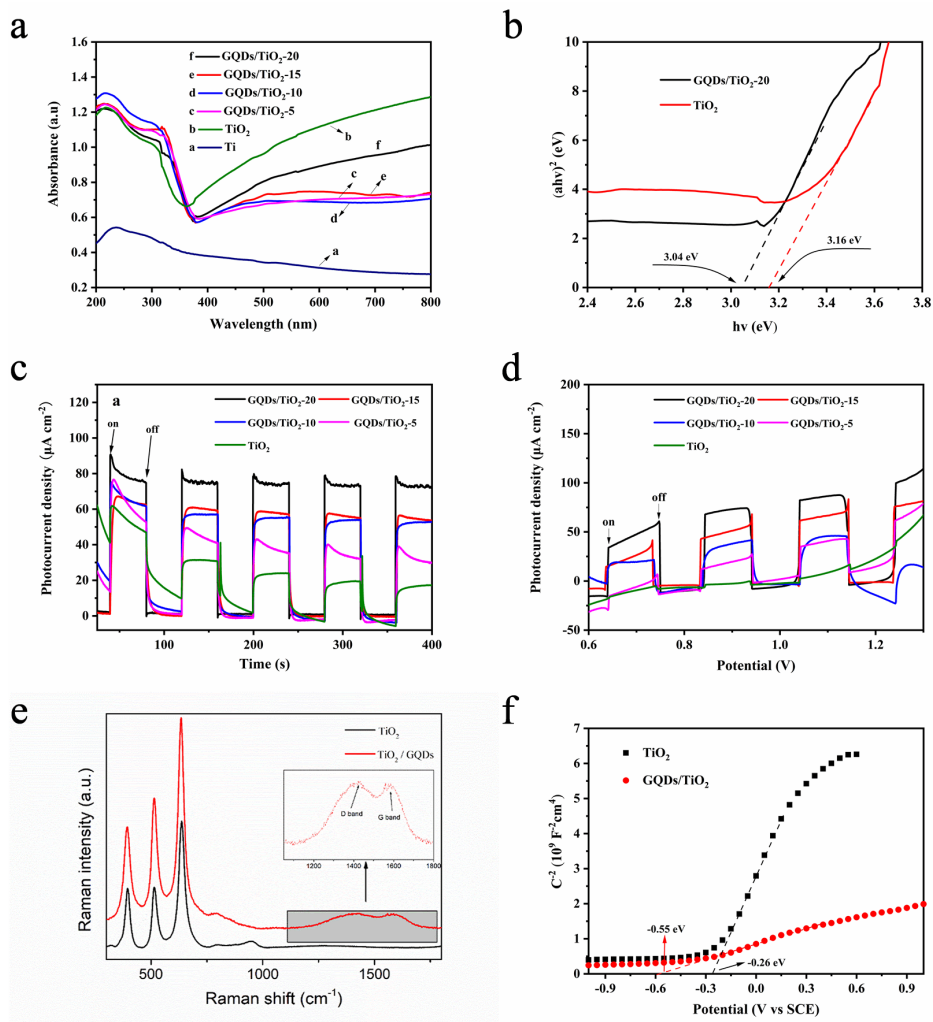


**Figure 5.** (a, b) UV-vis diffuse reflectance spectra of TiO<sub>2</sub> and GQDs/TiO<sub>2</sub> NTs. (c) The current-time curve of GQDs/TiO<sub>2</sub> NTs composites. The curves were measured at the bias potential of 0.5 V vs. SCE, and (d) Linear sweep voltammetry of GQDs/TiO<sub>2</sub> NTs composites. The curves were recorded from -0.2 to 0.8 V vs. SCE at a scan rate of 0.01 V s<sup>-1</sup>, (e) Raman spectra of TiO<sub>2</sub> and GQDs/TiO<sub>2</sub>. (f) Mott-Schottky plots of TiO<sub>2</sub> and GQDs/TiO<sub>2</sub>. The initial potential of the test is -1 V, the termination potential is 1 V, the step size is 5 mV, the frequency is 1000 Hz, and the amplitude is 0.01 V.

**Table1.** Comparison and summary of the photoelectrochemical performance of similar materials.

Photoanode Materials	Charge Carrier Density Nd (cm <sup>-3</sup> )	Enhancement rate of the current density of composite photoanode material	Reference
TiO <sub>2</sub> NTs	9.073×10 <sup>19</sup>	-	This work
GQDs/TiO <sub>2</sub> NTs	1.265×10 <sup>21</sup>	514%	This work
TiO <sub>2</sub> NRs@Ag@GQDs	6.1×10 <sup>19</sup>	-	[40]
rGQDs/Fe <sub>2</sub> O <sub>3</sub>	-	800%	[41]
Sn/TiO <sub>2</sub>	1.25×10 <sup>19</sup>	50%	[42]
Carbon Dots/ZnO	3.70×10 <sup>20</sup>	202%	[43]

#### 4. CONCLUSION

In summary, GQDs/TiO<sub>2</sub> composite nanotube arrays were prepared by graphene quantum dot-assisted anodization. Characterization by SEM, TEM, Raman spectroscopy, and Infrared spectroscopy confirmed that the GQDs were evenly incorporated into the TiO<sub>2</sub> nanotubes. The GQDs/TiO<sub>2</sub> nanocomposites exhibited 72 μA/cm<sup>2</sup> high photocurrent density, which is 5.14 times higher than that of pure TiO<sub>2</sub> nanotube arrays. And the charge carrier density of GQDs/TiO<sub>2</sub> is 13 times that of TiO<sub>2</sub>, suggesting that the construction of the heterojunction promoted the efficient separation of photogenerated carriers. Overall, GQDs/TiO<sub>2</sub> composite nanotube arrays performed excellent PEC responsiveness and stability. This study displays a new insight into developing TiO<sub>2</sub>-based photocatalysts for water oxidation under simulated sunlight.

#### ACKNOWLEDGMENTS

This work was supported by the National Natural Science Foundation of China (22062005, 22165005, U20A20128) and the Guangxi Science Fund for Distinguished Young Scholars (2019GXNSFFA245016).

#### References

1. W. Liu, P. Geng, S. Li, W. Liu, D. Fan, H. Lu, Z. Lu, Y. Liu, *Journal of Energy Chemistry*, 55 (2021) 17-24.
2. W. Liu, P. Geng, S. Li, R. Zhu, W. Liu, H. Lu, S. Chandrasekaran, Y. Pang, D. Fan, Y. Liu, *International Journal of Hydrogen Energy*, 45 (2020) 28576-28585.
3. S. Chandrasekaran, N. Li, Y. Zhuang, L. Sui, Z. Xiao, D. Fan, V. Aravindan, C. Bowen, H. Lu, Y. Liu, *Chemical Engineering Journal*, 431 (2022) 134073.
4. N. Zheng, X. He, W. Guo, Z. Hu, *Chinese Chemical Letters*, 32 (2021) 1993-1997.
5. A. Fujishima, K. Honda, *Nature*, 238 (1972) 37.
6. J. Li, Y. Lin, R. Chen, X. Zhu, D. Ye, Y. Yang, Y. Yu, D. Wang, Q. Liao, *Journal of Energy Storage*, 43 (2021) 103228.
7. R. Liu, Z. Sun, X. Song, Y. Zhang, L. Xu, L. Xi, *Applied Catalysis A: General*, 544 (2017) 137-144.
8. R. Wang, J. Bai, Y. Li, Q. Zeng, J. Li, B. Zhou, *Nano-Micro Letters*, 9 (2016) 14.

9. Y. Qu, X. Li, H. Zhang, R. Huang, W. Qi, R. Su, Z. He, *Journal of Hazardous Materials*, 429 (2022) 128310.
10. J. Li, Y. Huang, M. Su, Y. Xie, D. Chen, *Environmental Research*, 207 (2022) 112081.
11. M. Ma, H. Wang, H. Liu, *Chinese Chemical Letters*, 32 (2021) 3613-3618.
12. H. Maleki-Ghaleh, M. S. Shakeri, Z. Dargahi, M. Kavanlouei, H. Kaveh Garabagh, E. Moradpur-Tari, A. Yourdkhani, A. Fallah, A. Zarrabi, B. Koc, M. H. Siadati, *Materials Today Chemistry*, 24 (2022) 100820.
13. S. Chandrasekaran, C. Zhang, Y. Shu, H. Wang, S. Chen, T. Nesakumar Jebakumar Immanuel Edison, Y. Liu, N. Karthik, R. D. K. Misra, L. Deng, P. Yin, Y. Ge, O. A. Al-Hartomy, A. Al-Ghamdi, S. Wageh, P. Zhang, C. Bowen, Z. Han, *Coordination Chemistry Reviews*, 449 (2021) 214209.
14. B. Xie, X. Ning, S. Wei, J. Liu, J. Zhang, X. Lu, *Chinese Chemical Letters*, 32 (2021) 2279-2282.
15. S. Hoang, S. P. Berglund, N. T. Hahn, A. J. Bard, C. B. Mullins, *Journal of the American Chemical Society*, 134 (2014) 3659-3662.
16. C. Das, P. Roy, M. Yang, H. Jha, P. Schmuki, *Nanoscale*, 3 (2011) 3094-3096.
17. J. H. Park, S. Kim, A. J. Bard, *Nano Letters*, 6 (2006) 24-28.
18. X. Yang, A. Wolcott, G. Wang, A. Sobo, R. C. Fitzmorris, F. Qian, J. Z. Zhang, Y. Li, *Nano Letters*, 9 (2009) 2331.
19. J. Bian, C. Huang, L. Wang, T. Hung, W. A. Daoud, R. Zhang, *ACS applied materials & interfaces*, 6 (2014) 4883-4890.
20. M. Xu, P. Da, H. Wu, D. Zhao, G. Zheng, *Nano Letters*, 12 (2012) 1503-1508.
21. K. Pandi, M. Preeyanghaa, V. Vinesh, J. Madhavan, B. Neppolian, *Environmental Research*, 207 (2022) 112188.
22. Z. Li, W. Luo, M. Zhang, J. Feng, Z. Zou, *Energy & Environmental Science*, 6 (2012) 347-370.
23. H. P. Cong, X. C. Ren, P. Wang, S. H. Yu, *Energy & Environmental Science*, 6 (2013) 1185-1191.
24. B.-Y. Cheng, J.-S. Yang, H.-W. Cho, J.-J. Wu, *ACS applied materials & interfaces*, 8 (2016) 20032-20039.
25. S. S. M. Bhat, S. A. Pawar, D. Potphode, C.-K. Moon, J. M. Suh, C. Kim, S. Choi, D. S. Patil, J.-J. Kim, J. C. Shin, H. W. Jang, *Applied Catalysis B: Environmental*, 259 (2019) 118102.
26. D. Jiang, X. Du, D. Chen, L. Zhou, W. Chen, Y. Li, N. Hao, J. Qian, Q. Liu, K. Wang, *Biosensors & Bioelectronics*, 83 (2016) 149-155.
27. D. Li, J. Jia, Y. Zhang, N. Wang, X. Guo, X. Yu, *Journal of Hazardous Materials*, 315 (2016) 1-10.
28. H. Wang, W. Liang, Y. Liu, W. Zhang, D. Zhou, J. Wen, *Applied Surface Science*, 386 (2016) 255-261.
29. L. Wang, Y. Wang, T. Xu, H. Liao, C. Yao, Y. Liu, Z. Li, Z. Chen, D. Pan, L. Sun, *Nature communications*, 5 (2014) 1-9.
30. J. Lin, Y. Liu, Y. Liu, C. Huang, W. Liu, X. Mi, D. Fan, F. Fan, H. Lu, X. Chen, *ChemSusChem*, 12 (2019) 961-967.
31. W. Liu, Z. Xiao, S. Chandrasekaran, D. Fan, W. Li, H. Lu, Y. Liu, *ACS Applied Materials & Interfaces*, (2022).
32. E. H. Chung, S. M. Yu, S. R. Baek, E. K. Jang, H. J. Han, J. P. Kim, T. E. Hong, J. S. Bae, J. S. Jin, E. D. Jeong, *Journal of the Korean Physical Society*, 61 (2012) 924-927.
33. G. Rajender, P. K. Giri, *Journal of Materials Chemistry C*, 4 (2016) 10852-10865.
34. R. Panyathip, S. Sucharitakul, S. Phaduanghitidhada, A. Ngamjarurojana, P. Kumnorkaew, S. Choopun, *Molecules*, 26 (2021) 5484.
35. D. R. Baker, P. V. Kamat, *Advanced Functional Materials*, 19 (2009) 805-811.
36. C. Gómez-Navarro, R. T. Weitz, A. M. Bittner, M. Scolari, A. Mews, M. Burghard, K. Kern, *Nano Letters*, 7 (2014) 3499.
37. F. Zhan, J. Li, W. Li, Y. Liu, R. Xie, Y. Yang, Y. Li, Q. Chen, *International Journal of Hydrogen Energy*, 40 (2015) 6512-6520.

38. G. Wang, Y. Ling, D. A. Wheeler, K. E. N. George, K. Horsley, C. Heske, J. Z. Zhang, Y. Li, *Nano Letters*, 11 (2011) 3503.
39. G. Wang, H. Wang, Y. Ling, Y. Tang, X. Yang, R. C. Fitzmorris, C. Wang, J. Z. Zhang, Y. Li, *Nano Letters*, 11 (2011) 3026-3033.
40. A. J. Cowan, J. Tang, W. Leng, J. R. Durrant, D. R. Klug, *The Journal of Physical Chemistry C*, 114 (2010) 4208-4214.
41. W. Zhang, W. Wang, H. Shi, Y. Liang, J. Fu, M. Zhu, *Solar Energy Materials and Solar Cells*, 180 (2018) 25-33.
42. Z. Zeng, T. Li, Y.-B. Li, X.-C. Dai, M.-H. Huang, Y. He, G. Xiao, F.-X. Xiao, *Journal of Materials Chemistry A*, 6 (2018) 24686-24692

© 2022 The Authors. Published by ESG ([www.electrochemsci.org](http://www.electrochemsci.org)). This article is an open access article distributed under the terms and conditions of the Creative Commons Attribution license (<http://creativecommons.org/licenses/by/4.0/>).